

# Estimating the absolute flux distribution for a synchrotron X-ray beam using ionization-chamber measurements with various filters

Andrew W. Stevenson<sup>a,b,\*</sup> and Francesca Di Lillo<sup>c,d</sup>

<sup>a</sup>Australian Synchrotron, 800 Blackburn Road, Clayton, Victoria 3168, Australia, <sup>b</sup>CSIRO Manufacturing, Private Bag 10, Clayton South, Victoria 3169, Australia, <sup>c</sup>Department of Physics 'Ettore Pancini', Università di Napoli Federico II, Naples, Italy, and <sup>d</sup>INFN, Sezione di Napoli, Naples, Italy. \*Correspondence e-mail: andrew.stevenson@synchrotron.org.au

Received 21 February 2017

Accepted 20 June 2017

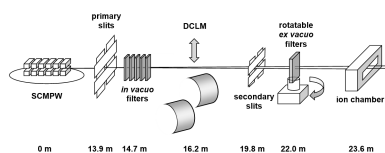
Edited by A. Momose, Tohoku University, Japan

**Keywords:** ionization chambers; filters; X-ray beam quality; harmonic contamination.

It is shown that an extensive set of accurate ionization-chamber measurements with a primary polychromatic synchrotron X-ray beam transmitted through various filter combinations/thicknesses can be used to quite effectively estimate the absolute flux distribution. The basic technique is simple but the 'inversion' of the raw data to extract the flux distribution is a fundamentally ill-posed problem. It is demonstrated, using data collected at the Imaging and Medical Beamline (IMBL) of the Australian Synchrotron, that the absolute flux can be quickly and reliably estimated if a suitable choice of filters is made. Results are presented as a function of the magnetic field (from 1.40 to 4.00 T) of the superconducting multi-pole wiggler insertion device installed at IMBL. A non-linear least-squares refinement of the data is used to estimate the incident flux distribution and then comparison is made with calculations from the programs *SPECTRA*, *XOP* and *spec.exe*. The technique described is important not only in estimating flux itself but also for a variety of other, derived, X-ray properties such as beam quality, power density and absorbed-dose rate. The applicability of the technique with a monochromatic X-ray beam for which there is significant harmonic contamination is also demonstrated. Whilst absolute results can also be derived in this monochromatic beam case, relative (integrated) flux values are sufficient for our primary aim of establishing reliable determinations of the percentages of the various harmonic components.

## 1. Introduction

The ability to reliably and accurately determine the flux distribution (as a function of energy) for a polychromatic X-ray beam has been the goal of several studies, for both laboratory-based and synchrotron sources. One approach is to develop a model enabling the calculation of such spectra. In some cases such models have been empirical or semi-empirical in nature [see, for example, in the case of laboratory sources, Boone & Seibert (1997) and Tucker *et al.* (1991), respectively]. The medical/biomedical research community in particular has developed extensive Monte Carlo-based simulations, to considerable advantage, *e.g.* Ay *et al.* (2004) and Flegontova *et al.* (2007). This work has been crucial with respect to calculating X-ray beam properties such as absorbed-dose rate, power density, weighted-average energy, half-value layers, and in the design/development of diagnostic imaging apparatus/procedures, including detectors and dosimeters (Meyer *et al.*, 2004)/beam-hardening corrections (Van de Casteele *et al.*, 2002). In the materials science field, and particularly associated with the use of scanning electron microscopy as a tool, Monte Carlo computer programs such as *Win X-ray* (Gauvin *et al.*, 2006) and *CASINO* (Drouin *et al.*, 2007) are widely used



for the calculation of X-ray spectra. A knowledge of the X-ray spectra is also very important for materials-composition analysis, such as is widely practiced using dual-energy tomography scanners (Gabbai *et al.*, 2015).

Features which distinguish typical laboratory-based and synchrotron spectra include the presence, in the former, of sharp characteristic lines and a distinct maximum X-ray energy (within the operative region).<sup>1</sup> X-ray spectra for laboratory-based sources depend not only on the chemical composition of the target or anode but also on its size, geometry and surface finish [see, for example, Nowotny & Höfer (1985)]. On the other hand, in the absence of any filters comprising elements with absorption edges within the operative region, both the underlying Bremsstrahlung spectrum for a laboratory source and synchrotron spectra typical of bending magnets or wiggler insertion devices are generally smooth and continuous in appearance.

Meyer *et al.* (2004), for example, have pointed out that directly measuring X-ray spectra, even for laboratory-based sources, is difficult due to the very high fluxes encountered. Fewell & Shuping (1977) have been pioneers in the use of spectrometer systems based on high-purity (intrinsic) Ge for such purposes. Compton scattering has been used as a means of circumventing the issue of excessive flux in the primary X-ray beam [see, for example, Gallardo *et al.* (2004)], as has the Si surface barrier detector (Pani *et al.*, 1987).<sup>2</sup> A number of other detectors have also been used including those based on: NaI (Tl) scintillation (Epp & Weiss, 1966); Xe proportional counter (Israel *et al.*, 1971<sup>3</sup>); Si (Li) (Cho *et al.*, 1978); Ge (Li) (Birch & Marshall, 1979); Si PIN diodes (Aoki & Koyama, 1989); CdTe and CdZnTe (Takahashi & Watanabe, 2001). A quite different (and absolute) approach is *via* accurate X-ray powder-diffraction intensity measurements and has been applied to both the integrated flux for characteristic lines (Honkimäki *et al.*, 1990) and the flux distribution for Bremsstrahlung (Honkimäki & Suortti, 1992).

Attempts to determine X-ray spectra from experimental transmission data obtained with various filters originates with the studies of Silberstein (1932, 1933), Bell (1936), Jones (1940) and Greening (1947, 1950). The fact that research is still being undertaken in this area after some 80 years [see, for example, Sidky *et al.* (2005) and Cao *et al.* (2016)] reflects the practical importance of the task and, unfortunately, that this ‘inversion’ problem is ill-posed [involving an ill-conditioned linear system of equations; see, for example, Greening (1963) and Baird (1981)] and so not straightforward. Archer *et al.* (1988) have also emphasized the fact that, whilst computational approaches are important and useful, ‘they provide only generalized spectra’, whereas ‘to determine the spectra from a

*particular x-ray unit, quantitative measurements made on that unit are required*’.

In this paper we will confine our attention to kilovoltage (/orthovoltage) X-rays generated at a synchrotron beamline, but considerable work has also been carried out with respect to megavoltage X-rays (such as those produced by a linear accelerator), *e.g.* Manciu *et al.* (2009). Starting with the Beer–Lambert law to describe the attenuation of a (narrow) monochromatic X-ray beam by a filter, it is straightforward to write the corresponding integral, with respect to wavelength or energy, for a polychromatic beam. Reformulating this result with the integration variable being instead the linear attenuation coefficient  $\mu$ , yields an integral immediately recognizable as a Laplace transform [see, for example, Silberstein (1932)]. The fact that the unknown X-ray spectra sought appear within the integral renders this an inhomogeneous Fredholm integral equation of the first kind, the solution of which is in general intrinsically unstable [see, for example, Tikhonov & Arsenine (1977)].

## 2. Experimental

The experimental results reported in this paper were collected at the Imaging and Medical Beamline (IMBL) of the Australian Synchrotron. The IMBL, which has extensive research and development capabilities in the broad areas of X-ray imaging, tomography and radiotherapy, has been described in detail by Stevenson *et al.* (2010, 2012, 2017) and utilizes a superconducting multi-pole wiggler (SCMPW), supplied by Budker Institute of Nuclear Physics (installed in July 2012). The SCMPW has (effectively)  $30 \times 5.2$  cm periods (total length 1.56 m) and a maximum magnetic field of 4.20 T. The ‘standard’ field at IMBL is 3.00 T, but 1.40, 2.00 and 4.00 T are also available for particular user applications. A conservative estimate of the error in the wiggler field is  $\pm 0.08$  T, based on Hall-probe measurements performed during both factory-acceptance and site-acceptance tests. Such measurements of the longitudinal magnetic field distribution, at particular set fields relevant to IMBL operation, show excellent uniformity/periodicity along the entire length of the wiggler. Corresponding plots of spectral power as a function of spatial frequency show the contribution from the third-order harmonic decreasing from approximately 2.2% at 1.50 T (3.4% at 1.00 T) to approximately 0.37% at 4.00 T (0.34% at 4.20 T).

### 2.1. Pink beam

The X-ray beam(s) used for the majority of the present work has a small cross-section [ $1.1$  mm (H)  $\times$   $0.8$  mm (V) at  $23.6$  m from the source<sup>4</sup>] and so ‘roll-off’ effects will be ignored; such effects have been addressed at length, especially for larger beams, by Stevenson *et al.* (2017). Fig. 1 shows a schematic diagram of the basic experimental arrangement used in this study. The *in vacuo* filter vessel has five inde-

<sup>1</sup> Synchrotron spectra can of course also include sharp lines when insertion devices such as undulators are employed.

<sup>2</sup> Such devices are usually used for the detection of charged particles and have extremely low efficiency for kilovoltage X-rays, a distinct advantage in this case.

<sup>3</sup> Includes a comparison of NaI (Tl), Si (Li), Ge (Li) and Xe detectors, the latter proportional counter employs a gas mixture of 95% Xe and 5% N<sub>2</sub> at atmospheric pressure.

<sup>4</sup> As measured from Gafchromic<sup>®</sup>-film exposures recorded at the ionization-chamber position.

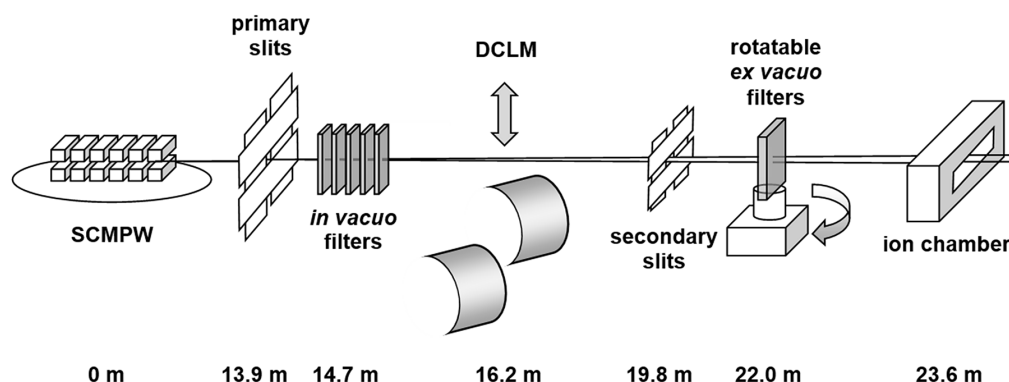


Figure 1

Schematic diagram of the experimental arrangement used. The primary (high-heat-load) slits and *in vacuo* filter vessel are located in hutch 1A and centred at 13.9 and 14.7 m from the source (SCMPW), respectively. In hutch 1B the (*in vacuo*) secondary slits are centred at 19.8 m, the rotatable *ex vacuo* filter stage is at 22.0 m, and the IC is at 23.6 m. The ‘filter angle’ ( $\varphi$ ) is defined as the angle between the X-ray beam direction and the normal to the plane of the filter. We also implicitly assume that both of these directions lie in the horizontal plane. The DCLM is also shown, centred at 16.2 m and located in hutch 1A. When the DCLM is translated vertically into the beam the resulting doubly diffracted, monochromatic beam is offset by 20 mm and so downstream components must be raised by 20 mm too. Further details are provided in the text.

pendent filter paddles and, during radiotherapy experiments for example, might typically house 0.45 mm graphene, 5 mm high-density graphite, 10 mm high-density graphite, 1 mm Cu and 1 mm Cu from upstream to downstream. The first (upstream) paddle has a nominal filter angle ( $\varphi$ ) of  $0^\circ$  and the other four of  $45^\circ$ , *i.e.* the total, nominal Cu thickness, as seen by the X-ray beam, would actually be  $2\sqrt{2}$  mm; a more detailed description and characterization of these filters is provided by Stevenson *et al.* (2017). In the present case the two paddles (4 and 5) which are furthest downstream each have, instead of 1 mm Cu, 2 mm Al, *i.e.* a total, as seen by the X-ray beam, of  $4\sqrt{2}$  mm Al. Such a filter train is typical of that used at IMBL during imaging and tomography experiments. The (free-air, parallel-plate) ionization chamber (IC) is a model ADC IC-105, with a plate length (in the beam direction) of  $L = 5$  cm and a plate separation (vertical and perpendicular to the beam direction) of 1.425 cm. This IC was operated without windows and the applied high voltage was 2 kV.

Other optical elements in the path of the X-ray beam and not shown in Fig. 1 are: 0.6 mm-thick diamond filter (not a vacuum window; CVD; Applied Diamond Inc.) in the front-end (FE), at 8.2 m; 0.35 mm-thick Be window at 21.2 m (hutch 1B), with associated 74 mm He path and 38  $\mu\text{m}$ -thick Al foil; Pb (anti-scatter) screens with approximately 20 mm-diameter circular apertures (centred on the X-ray beam) at 21.6 m and 22.6 m, *i.e.* upstream and downstream of the rotation stage for the *ex vacuo* filters.

The actual storage-ring energy for these experiments was 3.033 GeV and the nominal ring current was 10 mA (this was facilitated by performing the experiments during ‘machine studies’ rather than normal ‘user-beam’ time). This low ring current<sup>5</sup> is delivered *via* ‘decay’ rather than ‘top-up’ mode; however, with such a low ring current the lifetime of the beam

is quite long and so this decay is very gradual. The main reason for operating with a lower ring current is to avoid the problem of ion-recombination effects in the ADC IC (Stevenson *et al.*, 2017). The ‘offset’ current is usually of order 50  $\mu\text{A}$  or less, representing at most 0.5% of the nominal ring current, and so can be justifiably ignored in the present case. The average values of air temperature and pressure in the experimental hutch (1B), during the pink-beam experiments, were 23.8 (0.3) $^\circ\text{C}$  and 101190 (120) Pa, respectively. The ionization current from the ADC IC is read out *via* a Keithley 6487 picoammeter and the absolute value of the background reading, in the absence of an X-ray beam, is typically  $\sim 10^{-13}$  A.

Two supplementary pink-beam experiments conducted in IMBL hutch 3B and also employing a PinPoint ionization chamber will be described in detail in §4.1 and Appendix A.

## 2.2. Monochromatic beam

In the case of the monochromatic beam work presented here, the double-crystal Laue monochromator (DCLM) is introduced, as shown schematically in Fig. 1. The two 1.00 mm-thick Si crystals are both bent (meridionally; assumed cylindrically; concave from the point-of-view of the incoming X-ray beam), with an approximate radius of curvature of 10 m. The introduction of the DCLM necessitates raising the height of all downstream elements by the monochromatic beam offset, namely 20 mm. The DCLM was set to diffract X-rays of energy 25.3 (0.1) keV<sup>6</sup> from the Si(111) Bragg planes and the associated first-crystal rocking curve had a FWHM of approximately 17 arcsec.

The X-ray beam used in the present work has a cross section of 5.8 mm (H)  $\times$  2.1 mm (V) at 23.6 m from the source. The

<sup>5</sup> Normal ‘top-up’ mode operation involves the ring current varying between 200.0 and 200.5 mA.

<sup>6</sup> The X-ray energy calibration had previously been established by using nine different foils with *K*-absorption edges from 20.0 keV (Mo) to 88.0 keV (Pb), with 25.5 keV (Ag) being the closest to the present case.

SCMPW field was 4.00 T throughout this monochromatic beam work. The average values of air temperature and pressure in the experimental hutch (1B), during the monochromatic beam experiments, were 24.0 (0.1)°C and 101720 (120) Pa, respectively. Other experimental details are as in §2.1, with the exception that the nominal ring current was 50 mA (again during ‘machine studies’ rather than normal ‘user-beam’ time).<sup>7</sup>

### 3. Methods

#### 3.1. Pink beam

Data were collected for four SCMPW fields (1.40, 2.00, 3.00 and 4.00 T) and seven rotatable filters (0.5, 1.0, 2.0 and 4.0 mm Cu; 2.0 mm Al; 0.5 mm Al/30 µm Mo/0.5 mm Al; 0.5 mm Al/50 µm Au/0.5 mm Al)<sup>8</sup>, *i.e.* a total of 28 scans. ‘Blank’ scans (no rotatable filter) were also collected at the beginning and end of each wiggler-field set. The scans went from –80° to +80° in 2° steps<sup>9</sup>, about the vertical rotation axis. The small horizontal dimension of the X-ray beam (1.1 mm at the IC) ensures that these filters are large enough to fully intercept the beam at the largest filter angles, *e.g.* with an angle of ±80°, the foreshortening factor for the (apparent) filter width, as seen by the incident X-ray beam, is approximately 6. All of the filter materials used here are at least 100 mm in the horizontal direction. In the cases of the thinner, high-atomic-number filters, Mo and Au, the role of the Al (in the form of two 0.5 mm-thick filters on either side) is largely one of support and protection; however, the X-ray attenuation of this thin Al must of course, also be accounted for rigorously.

We have already discussed the ill-posed nature of the basic problem being tackled here and Cao *et al.* (2016), for example, have also discussed the contributing factor of having a large number of unknowns to be determined and a relatively small number of measurements with which to undertake this task. We will attempt to address this unfavourable situation by decreasing the former, through the least-squares refinement of a small number of key parameter values used to describe the shape of the flux distribution, and increasing the latter, by using the rotatable filters to efficiently generate a more extensive and comprehensive experimental data set.

In processing the data for each scan, individual values of IC current are scaled by the ratio of the average ring current for the whole scan and the corresponding individual ring-current values. The seven processed data files (corresponding to the seven different rotatable filter combinations) for a given SCMPW field are then supplied as input to a non-linear least-

squares refinement program. This program employs a finite-difference algorithm, based on the work of Levenberg (1944) and Marquardt (1963), to fit experimental and calculated values of IC current (by varying parameters which describe the flux distribution). The calculated values can be given (in units of A, for a particular value of  $\varphi$ , and assuming a constant flux and continuous radiation) by

$$I_{\text{TOT}} = \frac{10^6 \delta E Q}{W_{\text{air}}} \times \sum_{E=E_{\text{start}}, \delta E}^{E_{\text{end}}} \frac{\Psi(E) T(E, \varphi) \{1 - \exp[-\mu_{\text{m, en}}(E) \rho_{\text{air}} L]\}}{K_e(E)}, \quad (1)$$

where  $\delta E$  is the energy increment in keV,  $Q = 1.602176565 \times 10^{-19}$  C is the elementary (electron) charge,  $\Psi(E)$  is the flux at X-ray energy  $E$  in photons  $\text{s}^{-1}$  (0.1% bandwidth)<sup>-1</sup>,  $T(E, \varphi)$  is the (dimensionless) transmission factor for the relevant (rotated and fixed) filters,  $\mu_{\text{m, en}}(E)$  is the energy-dependent mass energy-absorption coefficient of air in  $\text{cm}^2 \text{g}^{-1}$ ,  $\rho_{\text{air}}$  is the density of ambient air in  $\text{g cm}^{-3}$ ,  $L = 5$  cm is the IC plate length (see §2.1),  $W_{\text{air}} = 33.97$  (0.05) eV [see, for example, Attix (1986) and Podgorsak (2005)] is the average energy required to create an ion pair in air, and  $K_e(E)$  is the (dimensionless) energy-dependent electron-loss correction factor for the IC.

In this study we use values of  $\mu_{\text{m, en}}(E)$  derived by logarithmic interpolation of data from the NIST database (see Hubbell & Seltzer, 1995), from  $E_{\text{start}} = 1$  keV to  $E_{\text{end}} = 1000$  keV in steps of  $\delta E = 0.1$  keV. If we denote the air density at standard temperature and pressure (STP) used by NIST (20°C and 101325 Pa) as  $\rho_{\text{air, STP}} = 0.001205$   $\text{g cm}^{-3}$ , then the appropriate correction (based on the ideal gas law) for other temperatures ( $T$ ) and pressures ( $P$ ) is

$$\rho_{\text{air}} = \rho_{\text{air, STP}} \left( \frac{293.15}{T} \right) \left( \frac{P}{101325} \right) = \rho_{\text{air, STP}} / K_{\text{TP}}. \quad (2)$$

Thus  $K_e(E)$  and  $K_{\text{TP}}$  are the only IC correction factors we will need to consider here. Stevenson *et al.* (2017) discussed other such correction factors at length, especially  $K_s$  for ion recombination. However, as mentioned in §2.1, the use of low ring current in the present study ensures that  $K_s$  can be neglected, *i.e.* is essentially unity. The values of  $K_e(E)$  used here are as described in detail by Stevenson *et al.* (2017) and are based on Monte Carlo calculations performed specifically for the ADC IC.

It is important to realise that in this study we do not include any arbitrary scale factors nor are we dealing with relative quantities (such as ‘ $I/I_0$ ’). The data are treated with a view to extracting estimates of the *absolute* flux distribution [ $\Psi(E)$ ].<sup>10</sup> We have some flexibility in our choice of the spectrum to be determined/refined. For example, it might be the spectrum immediately after the diamond filter in the FE, or after the carbon-based *in vacuo* filters, or after all of the *in vacuo* filters

<sup>7</sup> The accelerator operators ran a script which ensured that the ring current remained between 50.1 and 50.4 mA throughout, *i.e.* a pseudo ‘top-up’ mode operation.

<sup>8</sup> The filters used were: Al and Cu, Gammex 115A and 116 HVL attenuator sets, respectively; Mo, Goodfellow Cambridge Ltd, 99.9% purity, temper – annealed; Au, Advent Research Materials Ltd, 99.99% purity, temper – as rolled. The importance of using such high-quality/-purity filter materials in the present case has been investigated by, for example, Hübner (1958), Jones (1961) and Archer *et al.* (1988).

<sup>9</sup> Small corrections (angular offsets) were made on the basis of peak-shape fitting to establish the true 0° position for each scan.

<sup>10</sup> The  $\Psi(E)$  distribution involved is that for 200 mA storage-ring current and the calculations of  $I_{\text{TOT}}$  involve a scaling by the ratio of the average ring current for a whole scan and 200 mA.

(including the Al); we have chosen the latter in order to avoid the situation of attempting to ‘retrieve’ parts of the spectrum which never actually have any influence on the measurements. The calculation of values of  $I_{\text{TOT}}$  as outlined above needs to be robust, accurate and reliable; if our model has a significant deficiency, this is likely to manifest itself as some deleterious component which is convoluted with the true flux distribution we seek. The experimental values of  $I_{\text{TOT}}$ , for a given SCMPW field, can vary over several orders of magnitude (more than four in the case of 1.40 T; from  $\sim 10^{-12}$  A to almost  $10^{-7}$  A). In order to ensure that the least-squares refinement process is not biased, by way of being heavily influenced by just a small subset of the input experimental data, we actually minimize the following quantity,

$$\sum_i \{\log_{10}[I_{\text{TOT},i}(\text{expt})] - \log_{10}[I_{\text{TOT},i}(\text{calc})]\}^2, \quad (3)$$

where the summation extends over all of the data in the seven processed data files. This can be considered, in some sense, as the application of a weighting scheme. The agreement factor which we use is based on Hamilton’s *R*-factor (Hamilton, 1965), as frequently used in the field of crystallography, and defined as

$$\mathfrak{R} = 100 \left( \frac{\sum_i \{\log_{10}[I_{\text{TOT},i}(\text{expt})] - \log_{10}[I_{\text{TOT},i}(\text{calc})]\}^2}{\sum_i \{\log_{10}[I_{\text{TOT},i}(\text{expt})]\}^2} \right)^{1/2} \% \quad (4)$$

We need to specify certain parameters, which can be varied during the least-squares refinement process, to describe the  $\Psi(E)$  distribution. Our aim is to determine the absolute flux distribution(s) in a manner which avoids bias or the application of, possibly erroneous, preconceived ideas.<sup>11</sup> Therefore, with a minimum of constraints imposed, we have chosen to fit  $\Psi(E)$  with a single split Pearson VII function (Pearson, 1916), as follows:

$$\Psi(E) = P \left[ 1 + \frac{(E - E_{\text{peak}})^2}{m_{\text{low}} \omega_{\text{low}}^2} \right]^{-m_{\text{low}}}, \quad E < E_{\text{peak}}, \quad (5)$$

$$\Psi(E) = P \left[ 1 + \frac{(E - E_{\text{peak}})^2}{m_{\text{high}} \omega_{\text{high}}^2} \right]^{-m_{\text{high}}}, \quad E \geq E_{\text{peak}}.$$

The Pearson VII function is widely used, *e.g.* for fitting peak profiles in Rietveld refinement of powder-diffraction data (Young & Wiles, 1982). In the field of astronomy, it is known as the Moffat function (Moffat, 1969) and is used to describe stellar images, with the peak-shape parameter  $m$  being known as the ‘atmospheric scattering coefficient’. Equation (5) involves a total of six refinable parameters: the peak height  $P$  and position in energy  $E_{\text{peak}}$ ; the peak-shape parameters for

the low- and high-energy sides of the peak,  $m_{\text{low}}$  and  $m_{\text{high}}$ , respectively; the peak-width parameters for the low- and high-energy sides of the peak,  $\omega_{\text{low}}$  and  $\omega_{\text{high}}$ , respectively. The true values of these parameters, when expressed in terms of practical units [such as photons  $\text{s}^{-1}$  (0.1% bandwidth) $^{-1}$  for  $P$  and keV for  $E_{\text{peak}}$ ] can differ from one another by very large amounts/factors indeed and so we employ scaling factors to ensure that the refined values are of the same order of magnitude and the least-squares refinement proceeds efficiently and equitably. If a peak-shape parameter (no splitting of the peak) is unity ( $m = 1$ ) the associated functional form becomes  $P/[1 + (E - E_{\text{peak}})^2/\omega^2]$ , *i.e.* a Lorentzian (or Cauchy).<sup>12</sup> If a binomial expansion is applied to the general functional form and then we take the limit  $m \rightarrow \infty$ , the resulting series can immediately be recognized as  $P \exp[-(E - E_{\text{peak}})^2/\omega^2]$ , *i.e.* a Gaussian. It is straightforward to show that the FWHM  $F$  for the general functional form is given by  $2\omega[m(2^{1/m} - 1)]^{1/2}$ , which is  $2\omega$  for the case of a Lorentzian ( $m = 1$ ) and  $2\omega\sqrt{\ln 2}$  for a Gaussian ( $m \rightarrow \infty$ ). Another useful (dimensionless) parameter (for a split peak),  $\beta$ , is the ratio of the FWHM for the (half-) peak on the high-energy side to that on the low-energy side, *i.e.*  $F_{\text{high}}/F_{\text{low}}$ , with  $F = (F_{\text{low}} + F_{\text{high}})/2$ . This parameter provides a convenient measure of the degree of asymmetry of the derived spectrum, with  $\beta < 1$  meaning the spectrum is broader on the low-energy side,  $\beta = 1$  for a (pseudo-) symmetric<sup>13</sup> spectrum, and  $\beta > 1$  for the high-energy side being broader.

Fig. 2 shows, for demonstration purposes, examples of profiles obtained using (5). As we will see, an ability to combine different low-energy and high-energy functional forms is of particular relevance here, *e.g.* a Gaussian for  $E < E_{\text{peak}}$  and a Lorentzian for  $E \geq E_{\text{peak}}$ . Extra profiles obtained by including a (low-energy) damping function will be discussed in §4.1.

### 3.2. Monochromatic beam

In the case of the main monochromatic beam experiment, extensive ADC IC-current data were collected for six fixed *ex vacuo* Cu-filter thicknesses (0, 0.1, 0.25, 0.5, 1.0 and 2.0 mm) and seven rotatable filters (0.1 and 0.25 mm Cu; 2.0 and 5.0 mm Al; 0.5 mm Al/30  $\mu\text{m}$  Mo/0.5 mm Al; 0.5 mm Al/75  $\mu\text{m}$  Mo/0.5 mm Al; 0.5 mm Al/50  $\mu\text{m}$  Au/0.5 mm Al), *i.e.* a total of 42 scans. ‘Blank’ scans (no rotatable filter) were also collected at the beginning and end of each fixed-filter set. The fixed Cu filters were placed at approximately 21.4 m from the X-ray source, between the Be window and the upstream Pb screen (see §2.1 and Fig. 1). These filters serve to ensure that the full data set has sensitivity to the presence of different harmonic contributions. This is analogous to the frequent situation in crystallography where comprehensive crystal-structure refinements rely on the (diffraction) intensity data including Bragg reflections over a wide range of Bragg angles. For

<sup>11</sup> However, we are cognizant of the need for some form of constraint as has been pointed out by Baird (1981): ‘Reliability requires that artifacts be eliminated by forcing spectra to assume some preconceived basic shape. That is, one must use the attenuation data in conjunction with a realistic model for  $N(E)$ ’, where  $N(E)$  here refers to the photon fluence per unit energy for an X-ray tube source.

<sup>12</sup> For a value of 1.5, the functional form is the so-called ‘intermediate’ Lorentzian, and, for a value of 2, the ‘modified’ Lorentzian.

<sup>13</sup> We have said ‘(pseudo-) symmetric’ here because, whilst  $F_{\text{high}} = F_{\text{low}}$  implies  $\beta = 1$ , we may still have  $m_{\text{high}} \neq m_{\text{low}}$  and  $\omega_{\text{high}} \neq \omega_{\text{low}}$ , *i.e.* the two peak shapes may be different in general.

example, low-angle data can be particularly sensitive to bonding effects (and the phenomenon of extinction), whereas high-angle data can yield information on atomic thermal vibrations (such as anharmonicity) [see, for example, McIntyre *et al.* (1980)]. The scans went from  $-80^\circ$  to  $+80^\circ$  in  $2^\circ$  steps, about the vertical rotation axis, and were processed in a similar way to that already described for the pink-beam data. Out of a possible  $6 \times 7 \times 81 = 3402$  experimental data points, we ended up with 3396 points after imposing a lower limit on the IC current of  $10^{-11}$  A (as was also done for the pink-beam data). The experimental IC-current values span more than two orders of magnitude.

## 4. Results

### 4.1. Pink beam

Table 1 shows the results of the least-squares refinements performed at each SCMPW field, beginning with the values for 1.40 T in the second column. Very large values of  $m_{\text{low}}$  and

**Table 1**

Least-squares refinement results for the four SCMPW fields.

Each refinement is based on the seven corresponding experimental data sets (rotatable filter combinations) described in the text, with the minimum IC current considered being  $10^{-11}$  A. The peak shape on the low-energy side has been constrained to be a Gaussian ( $m_{\text{low}} = \infty$ ) in each case. The values of  $F$  and  $\beta$  are derived from the  $\omega_{\text{low}}$ ,  $m_{\text{low}}$ ,  $\omega_{\text{high}}$  and  $m_{\text{high}}$  values. Estimated standard deviations are given, in parentheses, for refined and derived parameter values.

	1.40 T	2.00 T	3.00 T	4.00 T
$P$ [photons $\text{s}^{-1}$ (0.1% bandwidth) $^{-1}$ ]	$5.17 (0.06) \times 10^{10}$	$1.48 (0.01) \times 10^{11}$	$3.22 (0.02) \times 10^{11}$	$4.15 (0.03) \times 10^{11}$
$\omega_{\text{low}}$ (keV)	8.71 (0.68)	10.4 (0.5)	8.18 (0.54)	8.42 (0.80)
$m_{\text{low}}$	$\infty$	$\infty$	$\infty$	$\infty$
$E_{\text{peak}}$ (keV)	36.5 (0.5)	40.1 (0.4)	40.3 (0.5)	41.7 (0.7)
$\omega_{\text{high}}$ (keV)	20.1 (0.4)	25.7 (0.3)	37.2 (0.4)	47.3 (0.6)
$m_{\text{high}}$	4.66 (0.17)	3.69 (0.06)	3.30 (0.05)	2.89 (0.07)
$F$ (keV)	24.6 (0.7)	31.1 (0.5)	39.5 (0.6)	48.9 (0.9)
$\beta$	2.39 (0.19)	2.59 (0.13)	4.80 (0.32)	5.97 (0.57)
$\mathfrak{R}$ (%)	0.188	0.155	0.115	0.127

severe correlations with other refined parameters necessitated constraining this parameter value to  $\infty$ , *i.e.* a Gaussian peak shape on the low-energy side. The largest (other) correlations occurred between  $\omega_{\text{low}}$  and  $E_{\text{peak}}$ , and between  $\omega_{\text{high}}$  and  $m_{\text{high}}$ , with average (over the four refinements) correlation coefficients of 0.986 and 0.982, respectively. In order to check on the robustness and reproducibility of the results, using the 1.40 T data as a test case, we have performed various refinements with different starting values for the refined parameters. In particular, we began with the values provided in the second column of Table 1, except that those of (arguably) the most important parameters,  $P$  and  $E_{\text{peak}}$ , were multiplied by constants ranging from 0.001 to 2.5. In all of these cases, the final results obtained were as given in Table 1 (the number of least-squares refinement cycles varied from 31, for the multiplying constant being unity, to 112, when this constant was 2.5). Whilst such test results will depend on many factors including the treatment of the Hessian matrix, the means of calculating the Jacobian, and the exact least-squares convergence criterion applied<sup>14</sup>, they do confirm that the analysis is both robust and reproducible.

The values of  $P$  and  $E_{\text{peak}}$  increase systematically with increasing field as expected. Whilst the value of  $\omega_{\text{low}}$  shows little variation with field,  $\omega_{\text{high}}$  increases systematically, and  $m_{\text{high}}$  decreases systematically, *i.e.* the peak shape on the high-energy side is becoming more Lorentzian-like as the field increases. The values of the derived parameters  $F$  and  $\beta$  both increase systematically with field, *i.e.* the spectrum becomes broader and more asymmetric, as expected. The values of  $\mathfrak{R}$  are consistent with good fits between experimental and theoretical values of IC currents, as will be discussed below. In order to put these values into perspective, when a constraint is imposed for the 1.40 T data that the shape of the flux spectrum should be symmetric ( $m_{\text{low}} = m_{\text{high}}$  and  $\omega_{\text{low}} = \omega_{\text{high}}$ ), we obtain

<sup>14</sup> In our case the criterion is that, on successive least-squares cycles, refined-parameter values must agree, parameter by parameter, to four significant digits.

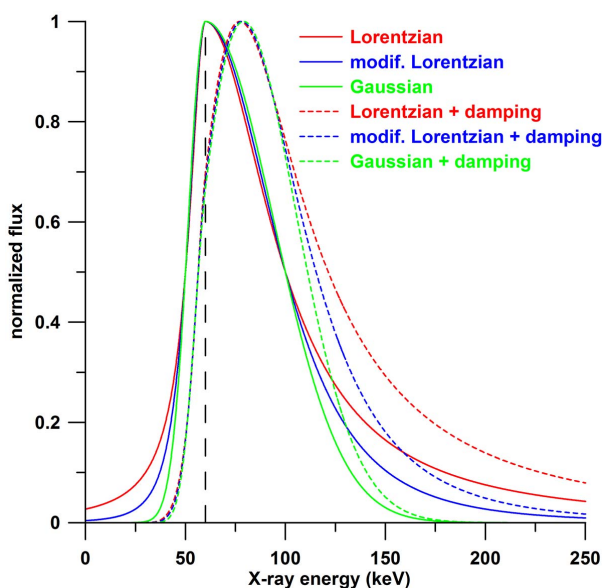


**Figure 2**

Calculated, normalized flux curves, based on (5), for demonstration purposes. The peak position ( $E_{\text{peak}}$ ) has been set to 60 keV (marked by the dashed vertical line), and  $m_{\text{low}} = m_{\text{high}} = 1$  (Lorentzian), 2 (modified Lorentzian) and  $\infty$  (Gaussian) as indicated.  $\omega_{\text{low}}$  has been chosen so that  $F_{\text{low}} = 20$  keV, and  $\omega_{\text{high}}$  so that  $F_{\text{high}} = 80$  keV, in each case, *i.e.*  $\beta = 4$  and  $F = 50$  keV. The damping function has the form  $\exp(-\text{const.}/E^3)$ , with the constant selected so that the function's value at 60 keV ( $E_{\text{peak}}$ ) is  $e^{-1}$ . The chosen form of the damping function incorporates the energy dependence associated with a linear absorption coefficient, photoelectric absorption being the dominant X-ray attenuation mechanism at the lower energies being considered here.

$\mathfrak{R} = 0.218\%$ , the further constraint that this symmetric peak should be Gaussian yields  $\mathfrak{R} = 0.554\%$  and that it be Lorentzian yields  $\mathfrak{R} = 1.52\%$ . Each of these cases results in concomitantly significant changes to the refined values of other parameters.

Figs. 3(a) and 3(b) show the experimental IC-current data and the calculated (least-squares) fits for the representative cases of 1.40 and 4.00 T, respectively. The agreement between experiment and calculation is clearly excellent across the full range of filtrations used. The IC currents span almost four orders of magnitude in each case. The corresponding flux distributions are shown in Fig. 4, together with results of calculations performed with *spec.exe* (Stevenson *et al.*, 2017). These calculations were performed using parameter values already provided above [1.1 mm (H)  $\times$  0.8 mm (V) at 23.6 m from the source; 3.033 GeV; 200 mA]. The spatial step size

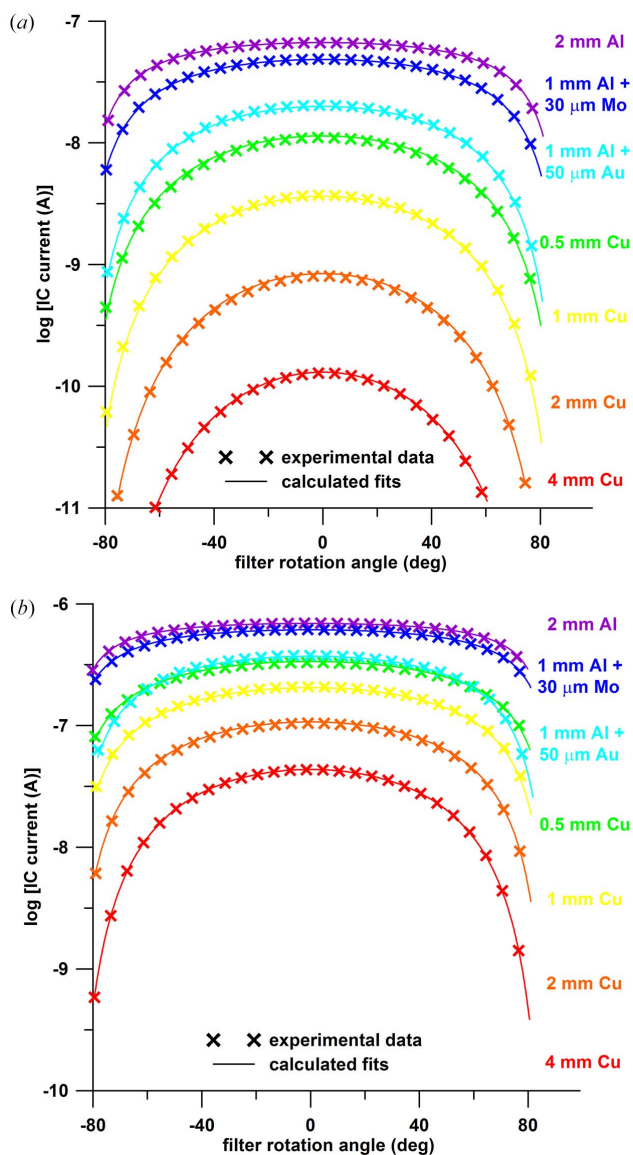


**Figure 3** Experimental data and the calculated (least-squares) fits for the (a) 1.40 T case and (b) 4.00 T case. Only every third data point is shown for clarity.

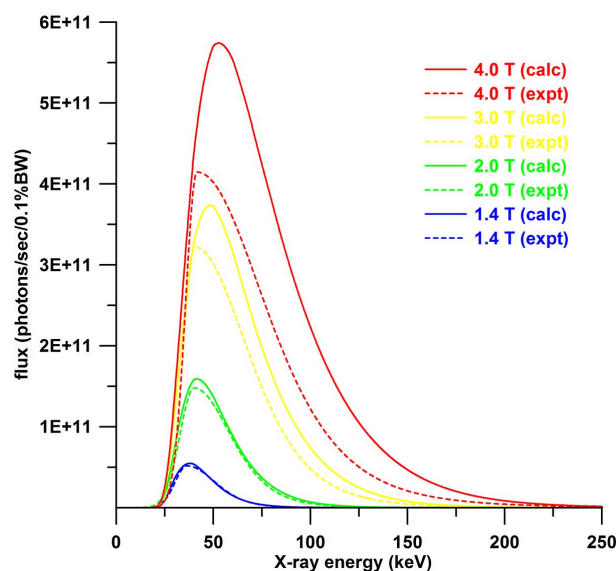


**Figure 4** Calculated and experimental flux distributions for the four SCMPW fields considered (1.40, 2.00, 3.00 and 4.00 T). The former have been calculated from first principles using *spec.exe* (Stevenson *et al.*, 2017) and the latter are as a result of the least-squares refinements of the experimental data, *i.e.* they are the spectra described by the parameter values given in Table 1. Further details are provided in the text.

across the beam cross-section was 5  $\mu\text{m}$  (horizontally and vertically) and the X-ray energy range was 1 to 1000 keV, in 0.1 keV steps (we only show results up to 250 keV in Fig. 4). The effects of (vertical) emittance are included. Allowance is made for all *in vacuo* filters already described.

In order to compare the *spec.exe* calculations with those of the well known programs *SPECTRA* (Tanaka & Kitamura, 2001, 2007) and *XOP* (Sánchez del Río & Dejus, 2011), Fig. 5 shows the relevant differences, as a function of X-ray energy, corresponding to Fig. 4. In the case of *SPECTRA* we have used version 9.0.2; ‘accuracy level’ set to 5. In the case of *XOP*, version 2.3; ‘WS (Wiggler Spectrum)’ and a spatial step size across the beam cross-section of 20  $\mu\text{m}$  (horizontally and vertically). The energy step is 0.1 keV (as above) and the curves in Fig. 5 are for running averages over nine data points. The agreement between the three programs is excellent, with all (absolute) differences being less than 0.6%.<sup>15</sup>

The salient features of the curves presented in Fig. 4 are quite obvious. The calculated and experimental flux distributions show excellent agreement for 1.40 T, and systematically poorer agreement as the SCMPW field increases, with the calculated values exceeding the experimental values. The shape of the experimental curves also becomes increasingly asymmetric or skewed (to a greater degree than the calculated curves) as the field increases. Notwithstanding the discrepancies, the results presented in Fig. 4 are impressive, especially in light of the inherent difficulties and ill-posed nature of the problem being addressed. Stevenson *et al.* (2017) have

<sup>15</sup> Note that we have quoted 0.6% rather than, say, 0.4% here, as the %-differences between *XOP* and *SPECTRA* flux values for the 1.40 T case (obtained by subtracting one blue curve from the other in Fig. 5) do approach 0.6%.

Table 2

Summary of key properties and derived quantities for flux distributions presented in Fig. 4, for the four SCMPW fields.

	1.40 T		2.00 T		3.00 T		4.00 T	
	expt	calc	expt	calc	expt	calc	expt	calc
$P$ [photons $s^{-1}$ (0.1% bandwidth) $^{-1}$ ]	$5.17 \times 10^{10}$	$5.47 \times 10^{10}$	$1.48 \times 10^{11}$	$1.59 \times 10^{11}$	$3.22 \times 10^{11}$	$3.74 \times 10^{11}$	$4.15 \times 10^{11}$	$5.74 \times 10^{11}$
$E_{\text{peak}}$ (keV)	36.5	37.9	40.1	41.4	40.3	48.6	41.7	52.6
$F$ (keV)	24.6	24.0	31.1	31.6	39.5	43.7	48.9	56.0
Weighted-average energy (keV)	41.4	41.2	46.9	47.1	54.4	55.8	60.7	63.7
Integrated flux (photons $s^{-1}$ )	$3.39 \times 10^{13}$	$3.53 \times 10^{13}$	$1.09 \times 10^{14}$	$1.19 \times 10^{14}$	$2.65 \times 10^{14}$	$3.31 \times 10^{14}$	$3.83 \times 10^{14}$	$5.75 \times 10^{14}$
Absorbed-dose rate to air ( $Gy s^{-1}$ )	2010	2060	5720	6060	12000	15200	16800	25500
Power (W)	0.225	0.233	0.821	0.897	2.31	2.96	3.72	5.87
Half-value layer (Al) (mm)	4.08	4.05	5.07	5.09	6.39	6.49	7.28	7.62
Half-value layer (Cu) (mm)	0.148	0.146	0.201	0.201	0.283	0.295	0.355	0.394

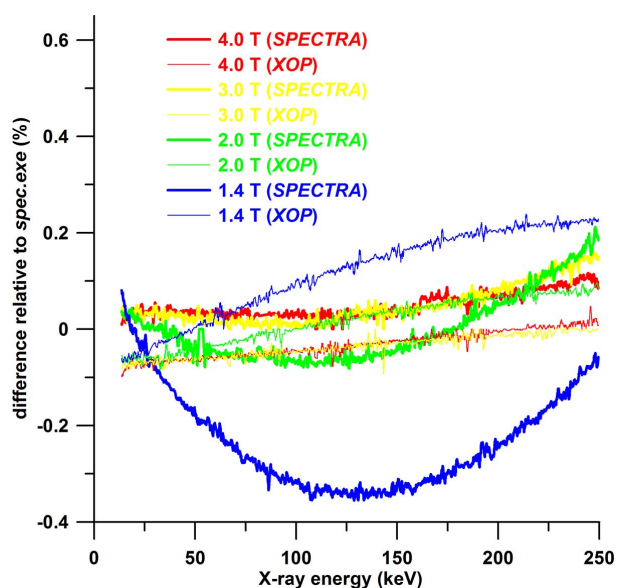


Figure 5

Comparison of calculated flux values, corresponding to Fig. 4, as a function of X-ray energy for the three computer programs *SPECTRA*, *XOP* and *spec.exe*, for the four SCMPW fields considered (1.40, 2.00, 3.00 and 4.00 T). The results are presented as %-differences relative to the *spec.exe* results. The minimum flux value considered was 1 photon  $s^{-1}$  (0.1% bandwidth) $^{-1}$  and running averages over nine data points have been used. Further details are provided in the text.

discussed at length the issue of comparing calculated and experimental flux distributions on an absolute scale, and obtained results quite consistent with those presented here. They also drew attention to the only other comparable study, that of Tanaka *et al.* (2000), where similar (but less comprehensive) trends were observed.

It is perhaps worth emphasizing/reiterating at this point that the least-squares refinements performed here relate specifically to fitting the experimental and calculated IC-current values (see Fig. 3), with the *experimental* flux distributions (see Fig. 4) being the product of this analysis. Merely fitting a single split Pearson VII function to, say, the (*spec.exe*) calculated flux distributions provided in Fig. 4 would be quite straightforward and undoubtedly yield excellent agreement. However, this would not provide any useful results nor insights. If we do actually try such fitting for the calculated 4.00 T flux curve in

Fig. 4, the results are as predicted in that we obtain a functional form which matches the solid red curve much more precisely than does the dashed red (experimental) curve. However, the corresponding calculated IC-current curves show much worse agreement with the experimental data than was the original case of Fig. 3(b), with the value of  $\mathfrak{R}$  increasing by a factor of approximately 30. This small test was in fact also quite instructive from the point of view that, whilst the (half-) peak on the high-energy side was fitted extremely well, the base of the (half-) peak on the low-energy side was more problematic. The attenuation of the low-energy X-rays is ‘faster’ (with decreasing  $E$ ) than can be satisfactorily described by even a Gaussian tail (let alone a Lorentzian tail). This is indeed borne out by the asymmetric experimental functional forms (as already mentioned above); the very rapid decrease of the X-ray flux with decreasing  $E$  results in a distortion of the fitted (in our case Gaussian) functional form and a concomitant *artificial* decrease of the value of  $E_{\text{peak}}$  (the value of  $F$  is also affected). This suggests that some other functional form might be more appropriate or that some extra (empirical) damping function could be applied. In Fig. 2 we have demonstrated the application of such a damping function; the rapid decrease of flux with decreasing  $E$  is more readily accommodated and the modified value of  $E_{\text{peak}}$  is more realistic. However, given that we have deliberately tried to avoid introducing any preconceived ideas of how the flux curves should appear, we will not pursue this line any further here.

Finally, we will briefly discuss the significance of the results presented in Fig. 4. Table 2 presents a summary of the values of key properties ( $P$ ,  $E_{\text{peak}}$  and  $F$ ) and derived quantities [weighted-average X-ray energy, integrated flux, absorbed-dose rate to air, power and half-value layer (HVL) for both Al and Cu] for experimental and calculated flux distributions at each of the four SCMPW fields. The experimental and calculated values of  $E_{\text{peak}}$  have discrepancies as a function of field as discussed above, whilst the weighted-average energy exhibits this trend to a considerably lesser extent as it is derived from the whole spectrum and so is less dependent on subtleties associated with peak position (this is also true to a certain extent for  $F$ ). The values of HVL, for both Al and Cu, being measures of the overall X-ray beam quality (in a similar way to the weighted-average energy), show generally good agree-

ment between experiment and theory. The remaining four items listed in Table 2 ( $P$ , integrated flux, absorbed-dose rate to air and power) all relate more directly to the *number* of X-rays in the beam, although the distribution with energy is still of course important. In the case of a given SCMPW field, the discrepancies between experiment and theory for these four items is reasonably consistent and the average %-difference of the calculated *versus* experimental values is 4.0, 8.0, 24 and 50% for 1.40, 2.00, 3.00 and 4.00 T, respectively. Interestingly, Stevenson *et al.* (2017) have pointed out a similar (in terms of sign and magnitude) such discrepancy in respect of absorbed-dose rates. They did not present a systematic trend with wiggler field, but did have evidence that the discrepancy increased with increasing hardness of the X-ray beam.

In order to investigate the source of this discrepancy, we collected some absolute dose-rate measurements, to compare with both *spec.exe* calculations and values derived from the experimental spectra in Fig. 4. The dose-rate measurements were obtained with a (PTB-) calibrated PTW Type 31014 PinPoint ionization chamber (S/N 1188; thimble geometry with measuring volume 15 mm<sup>3</sup>; Al electrode; operated at +400 V) in conjunction with a Type 10023 UNIDOS weblin dosimeter/electrometer. Since the recommended minimum field size for the PinPoint chamber is 20 mm × 20 mm and we wished to avoid the need to scan the chamber [that is, we wanted to perform static rather than dynamic measurements; see, for example, Livingstone *et al.* (2016)], we chose to conduct these experiments in IMBL's hutch 3B at 140 m from the source. This also had the beneficial effect of reducing the dose rate for our chosen *in vacuo* filter set, which was the same as has already been detailed previously. The maximum dose rate for the PinPoint chamber with continuous radiation and operating at +400 V, is 580.0 Gy s<sup>-1</sup> at 99.0% saturation and 265.5 Gy s<sup>-1</sup> at 99.5% saturation. Given that, with the SCMPW operating at 4.00 T, the dose rate for normal 200 mA 'top-up' mode might still be too high, we performed these experiments during 'machine studies' time with a special ring current of 19.7 mA. A 10 mm × 10 mm W mask (4 mm thick) was aligned in the X-ray beam at a distance of 137.7 m from the source, providing a 10.2 mm × 10.2 mm X-ray field at the PinPoint chamber position (140.0 m). Although somewhat smaller than the recommended field size for the PinPoint chamber, this is considerably larger than the chamber dimensions<sup>16</sup> and will already encompass significant roll-off effects in the vertical direction, as discussed below. The build-up cap was not used, in accord with the calibration certificate conditions for the relevant beam qualities.

<sup>16</sup> The PinPoint chamber has a basically cylindrical active region of volume 15 mm<sup>3</sup> and the chamber was disposed with this cylinder axis horizontal and perpendicular to the X-ray beam. This active region has a diameter of 2 mm, a length of 5 mm and a dome-shaped end; it includes the Al electrode.

Table 3

Details of absorbed-dose rate measurements and calculations for the four SCMPW fields, referred to 200.0 mA ring current.

Row	Details	1.40 T	2.00 T	3.00 T	4.00 T
#1	PinPoint chamber (Gy s <sup>-1</sup> )	37.7	113	261	373
#2	<i>spec.exe</i> (Gy s <sup>-1</sup> ) (10.2 mm × 10.2 mm field)	41.2	126	328	564
#3	<i>spec.exe</i> (Gy s <sup>-1</sup> ) [6.5 mm (H) × 4.7 mm (V) field]	44.0	133	341	584
#4	%-difference (#3 relative to #1)	16.7	17.7	30.7	56.6
#5	<i>spec.exe</i> (Gy s <sup>-1</sup> ) [5.0 mm (H) × 2.0 mm (V) field]	44.7	134	344	588
#6	Fig. 4 experimental data (Gy s <sup>-1</sup> )	42.2	123	269	383
#7	%-difference (#6 relative to #1)	11.9	8.85	3.07	2.68

Measurements of the accumulated charge (nC) over a period of 10 s were made three times and averaged. These values were then multiplied by the calibration factor for air Kerma (2.211 Gy nC<sup>-1</sup>). The multiplicative correction factor for beam quality  $K_O$  was applied [estimated to be 0.998, 0.993, 0.985 and 0.978 for 1.40, 2.00, 3.00 and 4.00 T, respectively; based on the Al and Cu HVL values in Table 2, and the PTB calibration certificate data provided for TH100 and TH140 beam qualities (see the clinical dosimetry standard DIN 6809-4)]. The correction factor  $K_{TP}$  for the true density of air [see (2)] was also applied; the value is 1.024, based on air temperature and pressure values of 22.3 (0.1)°C and 99700 (100) Pa. Finally, the values were scaled to 200.0 mA ring current (from 19.7 mA) and are shown in Table 3 (row #1). Row #2 of Table 3 shows the results of *spec.exe* calculations for the full 10.2 mm × 10.2 mm X-ray field [140.0 m from the source; 3.033 GeV; 200 mA]. The spatial step size across the beam cross-section was 25 μm (horizontally and vertically) and the X-ray energy range was 1 to 1000 keV, in 0.1 keV steps. The effects of (vertical) emittance are included. Allowance is made for all *in vacuo* filters already described, plus 0.205 m He, 4.8 m air, 2.7 mm Be and 0.114 mm Al [as detailed by Stevenson *et al.* (2017)]. This full X-ray field is considerably larger than the size of the PinPoint chamber and will encompass significant 'roll-off' effects in the vertical direction (see Stevenson *et al.*, 2017). Row #3 of Table 3, therefore, provides the *spec.exe* results for a 6.5 mm (H) × 4.7 mm (V) field, which represents the projection of the above 1.1 mm (H) × 0.8 mm (V) field at 23.6 m from the source, to 140.0 m. Comparing the dose rates in rows #2 and #3 clearly shows the effects of roll-off. Row #4 of Table 3 shows the %-differences for the smaller-field, calculated, dose rates relative to the PinPoint chamber measurements; clearly there is a systematic increase with SCMPW field.

We wish to use the experimental flux data from Fig. 4 to estimate the dose rates, but, in the interests of investigating any residual roll-off effects, row #5 of Table 3 provides the *spec.exe* results for a 5.0 mm (H) × 2.0 mm (V) field, this corresponding to the size of the PinPoint chamber. These results provide the reassurance that roll-off effects are of less significance in the two smaller X-ray fields considered, with differences between values in rows #3 and #5 being of order 1%. In order to demonstrate that the roll-off effects exhibited above are indeed in the vertical, rather than horizontal, direction, we calculated the dose rates for the 3.00 T case with

fields of 5.0 mm (H) × 10.2 mm (V) and 10.2 mm (H) × 2.0 mm (V), to yield 328 and 343 Gy s<sup>-1</sup>, respectively. The absorbed-dose rate ( $\dot{D}_0$ ) can be calculated according to the following equation:

$$\dot{D}_0 = \int \dot{D}_0(E) dE = \int \dot{\Psi}_{\text{fluence}}(E) \mu_{m,\text{en}}(E) dE, \quad (6)$$

where  $\dot{\Psi}_{\text{fluence}}(E)$ , the energy fluence rate for X-ray energy  $E$  at 140.0 m from the source, is derived from the experimental flux data in Fig. 4 [ $\Psi(E)$ ] by including the attenuation of 0.205 m He, 4.8 m air, 2.7 mm Be and 0.114 mm Al, and multiplying by  $(23.6/140.0)^2$  in accord with the inverse-square law. The results are given in row #6 of Table 3, and their %-differences relative to the PinPoint chamber measurements in row #7. These %-differences are greatly reduced in comparison with those in row #4, with the average value decreasing from 30.4% to 6.63%. These, significantly smaller, %-differences exhibit a systematic trend with SCMPW field, albeit now a decrease. It is also instructive to consider the accuracy we might associate with the PinPoint chamber measurements. A comparison between dose rates (surface absorbed-dose rates to water) measured at IMBL with an ADC IC-105 IC (operating, as in the present case, as a free-air chamber), a PTW 31014 PinPoint chamber, a PTW 34001 Roos chamber, and a graphite calorimeter (Harty *et al.*, 2014) was reported by Lye *et al.* (2016). If we treat the calorimeter as being, in some sense, the ‘gold standard’, then the IC results were between 3 and 5% higher, the Roos chamber results ~2% higher, and the PinPoint chamber results up to ~2% lower. This suggests that the dose rates in rows #1 and #6 of Table 3, whilst showing some remaining discrepancy for the 1.40 and 2.00 T cases, exhibit excellent agreement, within error, for the 3.00 and 4.00 T cases.

Appendix A provides details of further experimental and theoretical results obtained for both the ADC IC and the PinPoint chamber as a function of SCMPW field.

#### 4.2. Monochromatic beam

Whilst applying the rotating-filter approach, used above for pink beams, to a monochromatic X-ray beam might seem of limited use, we believe a low-energy beam which suffers from harmonic contamination is both an interesting and valuable test case. The 25.3 keV beam described in §2.2 will be our test case; there will undoubtedly be significant harmonic contamination especially with the SCMPW operating at 4.00 T. In order to demonstrate this we have recorded ADC IC-current measurements for transmission through pairs of Cu filters (of thicknesses  $t$  mm for  $I_0$  and  $t + 0.1$  mm for  $I$ ). In the case of a truly mono-energetic X-ray beam the value of  $I/I_0$  would remain constant, *i.e.* is independent of  $t$ . Fig. 6 shows the experimental results, together with calculated curves, for an ADC IC. The latter are for different percentages (in terms of integrated flux and relative to the total beam) of  $\lambda/3$  harmonic. It is also quite likely that higher-order harmonics are present but with relatively smaller contributions (we will discuss this possibility later). In general, the calculations are specific to the

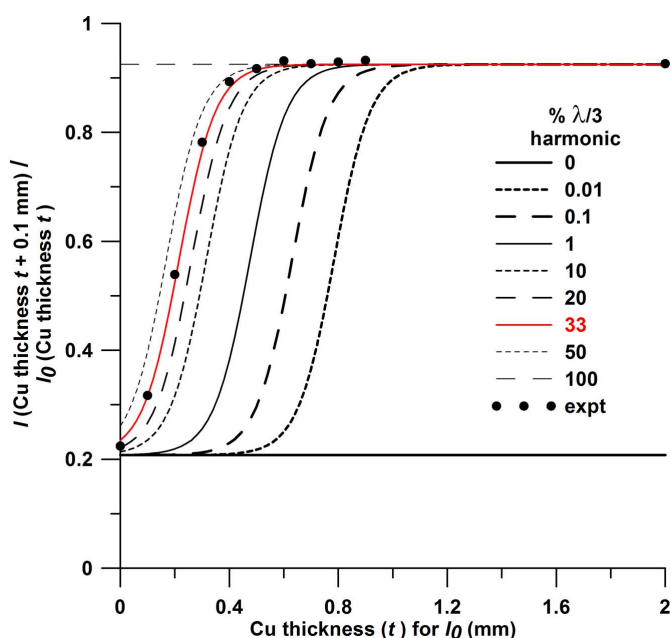


**Figure 6** Calculated monochromatic beam transmission ( $I/I_0$ ) curves for the ADC IC in the case of different levels of harmonic ( $\lambda/3$ ) contribution.  $I$  relates to the IC current after  $t + 0.1$  mm of Cu and  $I_0$  after  $t$  mm of Cu. Experimental results for a 25.3 keV monochromatic beam at IMBL are also shown. Further details are provided in the text.

ADC IC in that they must include parameters such as the IC plate length and electron-loss corrections, *i.e.* a monochromatic beam analogue of (1) is used [involving integrated flux (over  $E$ ) rather than flux]. These parameters are not involved in  $I/I_0$  for purely monochromatic beams, such as for the 0% and 100% curves in Fig. 6, shown as straight, horizontal lines. We see that the experimental results are in close accord with the calculated curve (shown in red) for 33%  $\lambda/3$  harmonic contamination.

Table 4 shows the results from the least-squares refinements of the main monochromatic beam data set, providing the evolution of the results as more refinable parameters (harmonic components) are included. The details of the least-squares refinement procedure are as given in §3.1, including the fact that the quantity minimized involves the logarithm of the individual experimental IC-current values [see (3)]. The energy of the fundamental component is one of the refined parameters (for all refinements) and the energies of higher-order harmonic components are the appropriate multiples of this energy. The integrated-flux values, given as a percentage of the total integrated flux for all harmonic components considered, are for the X-ray beam after the *in vacuo* filters, but upstream of the Be window and fixed Cu filter(s). The refinements, from #1 to #4, involve adding one extra harmonic contribution in each case. The refined value of the fundamental X-ray energy starts much higher than the ‘true’ value, reflecting in some sense a weighted-average value over the various harmonics which are in fact present but have not been acknowledged. This value decreases rapidly toward the expected value (25.3 keV). The value of the integrated flux for the  $\lambda/3$  harmonic from refinement #2 [33.4 (0.1)%] is in

excellent accord with the value of 33% obtained from Fig. 6 (red curve); note that #2 is the refinement directly comparable with the Fig. 6 result. Allowance for further higher-order harmonics sees the  $\lambda/3$  integrated-flux value decrease somewhat, as a percentage of the total integrated flux. The largest correlation-coefficient value and the  $\mathfrak{R}$ -value are also provided for each of the four refinements. As mentioned above, the integrated-flux values provided are those upstream of the fixed *ex vacuo* Cu filters; in order to demonstrate their effect, the integrated-flux values from refinement #4 in Table 4 become 0.0, 79.7, 7.8 and 12.5% for  $\lambda$ ,  $\lambda/3$ ,  $\lambda/4$  and  $\lambda/5$  harmonics, downstream of 2 mm Cu (neglecting the trivial effect of other elements such as the Be window).

On the other hand, for the X-ray beam immediately downstream of the DCLM (with the 0.6 mm-thick diamond being the only form of filtration), the integrated-flux values become 97.7, 2.1, 0.1 and 0.1% for  $\lambda$ ,  $\lambda/3$ ,  $\lambda/4$  and  $\lambda/5$  harmonics, respectively (based on the refinement #4 results in Table 4). In order to demonstrate that these values are quite reasonable, we used *spec.exe* to calculate the flux values for an X-ray beam of small cross section (assuming that roll-off effects are insignificant in this case), incident on the DCLM (at 16.2 m from the source). We then calculated the peak reflectivities, energy bandpasses and resulting integrated reflectivity for the DCLM, for each harmonic component, using the formalism developed by Erola *et al.* (1990) for the lamellar model of a bent crystal. This involves dividing the crystal into thin perfect-crystal slices of appropriately varying lattice spacing and orientation. The anisotropic elasticity of Si has been allowed for by using results from Schulze & Chapman (1995) and Schulze *et al.* (1998). Further details relating to these bent-crystal calculations are provided by Stevenson *et al.* (2017). Finally, the primary-beam flux values and DCLM integrated reflectivities are combined to yield values of integrated flux for each harmonic. The (percentage) results obtained are 96.9, 2.8, 0.3 and 0.0% for the  $\lambda$ ,  $\lambda/3$ ,  $\lambda/4$  and  $\lambda/5$  harmonics, respectively, in reasonable accord with the above, experimentally determined values.

Figs. 7(a) and 7(b) show the experimental IC-current data and the calculated (least-squares) fits (refinement #4) for the representative cases of 0 and 2.0 mm fixed *ex vacuo* Cu filters, respectively. There is generally very good agreement between experiment and calculation across the full range of rotatable filters used. The  $\mathfrak{R}$ -values given in Table 4 clearly show an improvement in the fit between experiment and theory as the number of harmonic components is increased. We did indeed also try a refinement with the next harmonic ( $\lambda/7$ ) included. However, this refinement (which yielded  $\mathfrak{R} = 0.100\%$ ) was not able to achieve our target convergence criterion (see §4.1) and so we have not included the results in Table 4. In this section,

**Table 4**

Least-squares refinement results for the monochromatic beam data.

Each of the four refinements (#1 to #4) includes one extra harmonic integrated-flux contribution in the theoretical model used to predict the IC currents. The integrated-flux values are given as a percentage of the total integrated flux for all harmonic components considered in each case.

	Refinement number			
	#1	#2	#3	#4
Energy (keV) ( $\lambda$ ) fundamental	69.2 (0.3)	26.05 (0.02)	25.48 (0.01)	25.24 (0.02)
Integrated flux (%) ( $\lambda$ ) fundamental	100.0 (1.5)	66.6 (0.2)	68.1 (0.2)	68.7 (0.2)
Integrated flux (%) ( $\lambda/3$ ) third harmonic	—	33.4 (0.1)	28.9 (0.1)	28.4 (0.1)
Integrated flux (%) ( $\lambda/4$ ) fourth harmonic	—	—	3.0 (0.1)	1.3 (0.1)
Integrated flux (%) ( $\lambda/5$ ) fifth harmonic	—	—	—	1.6 (0.1)
Largest correlation coefficient	0.761	0.869	0.770	0.928
$\mathfrak{R}$ (%)	1.82	0.183	0.107	0.102
Ratio $\mathfrak{R}_{\#(N-1)}:\mathfrak{R}_{\#N}$	—	9.97	1.70	1.06

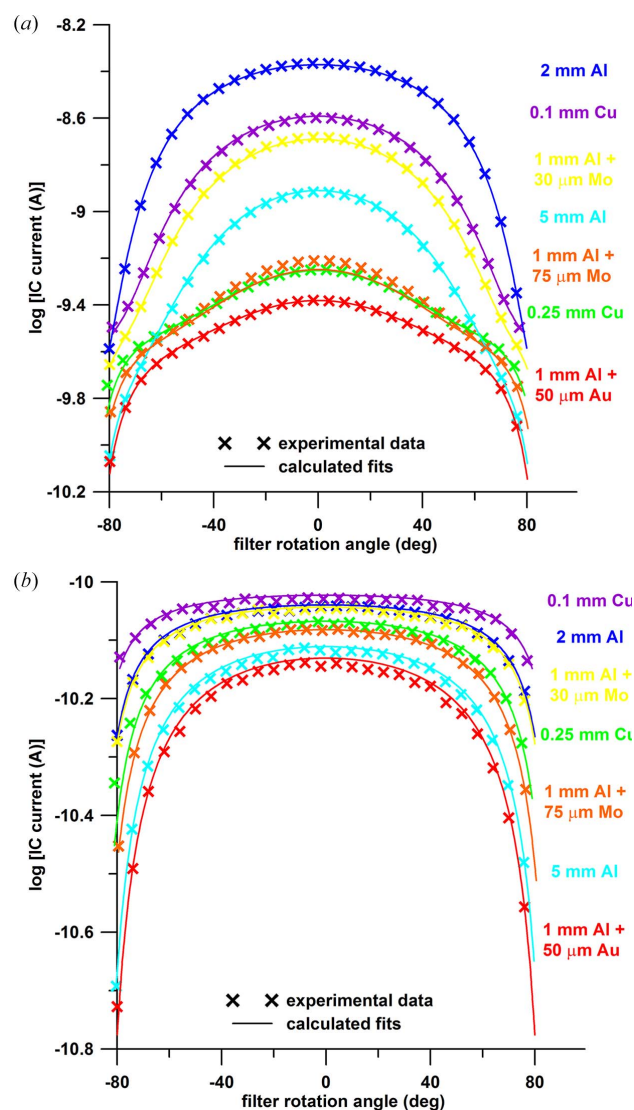


**Figure 7** Experimental data (monochromatic beam) and the calculated (least-squares) fits for the (a) 0 mm fixed *ex vacuo* Cu-filter case and (b) 2.0 mm fixed *ex vacuo* Cu-filter case. Only every third data point is shown for clarity.

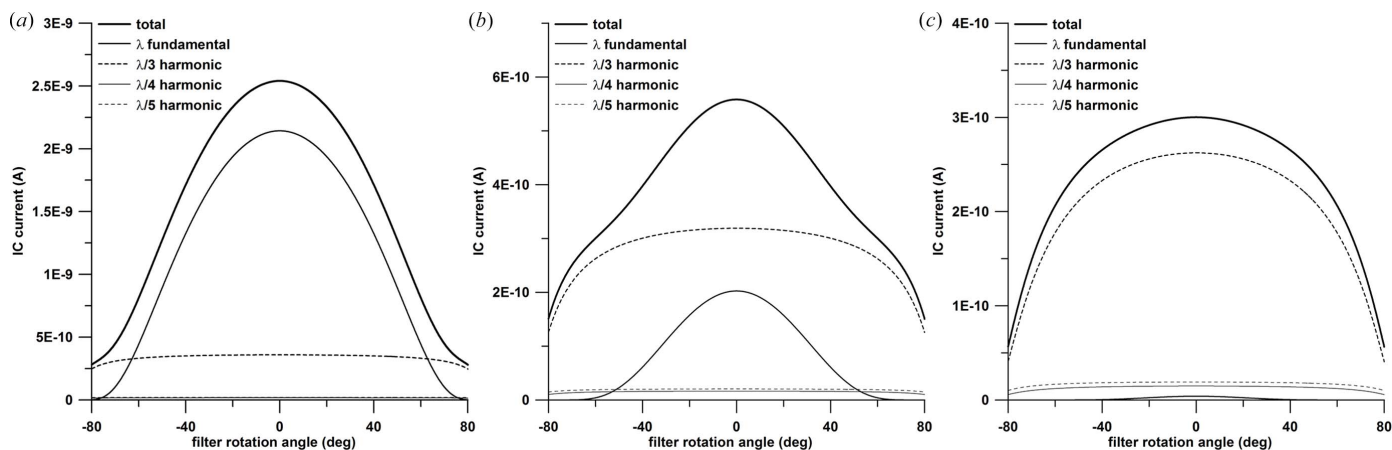


**Figure 8**  
 Calculated IC currents for the case of (a) a rotated 0.1 mm *ex vacuo* Cu filter, (b) a rotated 0.25 mm *ex vacuo* Cu filter and (c) a rotated 0.5 mm *ex vacuo* Cu filter. Individual curves are shown for each harmonic component and the total. Further details are provided in the text.

we have (implicitly) not considered the  $\lambda/2$  and  $\lambda/6$  harmonics, as these would arise from the ‘forbidden’ Si 222 and 666 Bragg reflections of the DCLM, respectively [see, for example, Stevenson *et al.* (2012)]. However, we did perform a test refinement, as for #4, but with allowance for a  $\lambda/2$  component. Again, the convergence criterion was not satisfied and  $\mathfrak{R} = 0.102\%$ . The values of the refined parameters were essentially unchanged from refinement #4 and the integrated-flux value for the  $\lambda/2$  component was zero within the associated error [0.004 (0.1)%].

Finally, we will discuss the improvement of the least-squares fits reported in Table 4 on a quantitative, rather than a qualitative, basis. The main aim is to objectively determine if the decrease of  $\mathfrak{R}$  in Table 4 does actually represent a *significant* improvement. Several authors have addressed such issues, especially in the field of crystallography, *e.g.* Cruickshank (1949). We will use the significance tests as provided by Hamilton (1965). The key parameters to be considered are the dimension of the hypothesis  $b$ , the number of degrees of freedom  $n - m$  (where  $n$  is the number of observations,  $m$  is the number of refined parameters, and  $n > m$ ), and the significance level  $\alpha$ . In comparing each refinement in Table 4 with the previous one, we have one extra refined parameter and so  $b = 1$ , and the value of  $m$  is 2, 3, 4 and 5 for #1, #2, #3 and #4, respectively. The issue of the value of  $n$  is less straightforward however; using  $n = 3396$  would result in all decreases of  $\mathfrak{R}$  being declared to be significant at the smallest value of  $\alpha$  considered by Hamilton (1965), namely 0.005 or 0.5%, *i.e.* ‘highly significant’ in the terminology of Hamilton (1964).<sup>17</sup> This is not reasonable and we cannot realistically consider using  $n = 3396$  to be the correct approach. On the other hand, using  $n = 42$ , the number of individual rotating-filter scans, is clearly overly conservative. As a compromise we have chosen to use  $n = 126$ , where we have assumed that three

observations can represent each individual rotating-filter scan, *e.g.* a peak height, width and shape parameter (such as was used in the above pink-beam study, with Pearson VII functional forms). It might be argued that even this is rather conservative, especially when we look at the variation and complexity of peak shapes evident in Figs. 7(a) and 7(b); we will return to this issue below. If we denote what Hamilton (1965) tabulates, and terms ‘significance points’, by  $S(b, n - m, \alpha)$ , we can use the recommended interpolation method to obtain values for  $S(1, 126 - m, 0.005)$  of 1.033 for  $m$ -values of 2, 3 or 4 and 1.034 for  $m = 5$ . The relevant  $R$ -factor ratios, given in the final row of Table 4, are all larger than these significance-point values and so all of the decreases in the values of  $\mathfrak{R}$  represent significant improvements [for the smallest value of  $\alpha$  considered by Hamilton (1965)], *i.e.* they are ‘highly significant’ in the terminology of Hamilton (1964).<sup>18</sup>

In order to further address the above-mentioned issue of the shapes of the curves obtained for IC current as a function of filter rotation angle, we present in Figs. 8(a), 8(b) and 8(c) the calculated such curves for 0.1, 0.25 and 0.5 mm of Cu being rotated, respectively. The IC currents are plotted on a linear scale here so that the way in which the subsidiary curves, for the separate harmonic components, combine to yield the total curve, can be seen more clearly and appreciated. The calculations have been performed with all of the aforementioned experimental conditions (including *in vacuo* and *ex vacuo* filtration, ring current, temperature, air pressure and so on) and the parameter values from least-squares refinement #4. As such, the 0.1 and 0.25 mm Cu curves have essentially already been presented in Fig. 7(a) (we did not collect data for the 0.5 mm Cu case). In the case of 0.1 mm Cu [Fig. 8(a)] the  $\lambda$  fundamental component dominates over the  $\lambda/3$  and other harmonics, resulting in the total curve being quite smooth and

<sup>17</sup> Hamilton (1964) advocates always quoting the actual value of the relevant significance level, but on p. 48 notes that the following are sometimes used: rejection at a significance level greater than 5% is ‘not significant’; rejection at a significance level of 5% is ‘significant’; rejection at a significance level of 1% is ‘highly significant’. See also p. 67 of Cruickshank (1949).

<sup>18</sup> If we do consider significance tests for the case of  $n = 42$  instead of  $n = 126$ , the conclusions remain unchanged for refinements #2 and #3. In the case of refinement #4, however, the decrease of  $\mathfrak{R}$ , relative to that for refinement #3, can only be said to be ‘significant’ in the terminology of Hamilton (1964), *i.e.*  $S(1, 37, 0.05)$  has the value 1.054 [ $S(1, 37, 0.025)$  has the value 1.072].

bell-shaped. On the other hand, in Fig. 8(c) the  $\lambda/3$  harmonic dominates and the total curve, whilst still smooth, is rather dome-shaped. In Fig. 8(b), the  $\lambda/3$  harmonic dominates at the larger filter-rotation angles, where the effective thickness of Cu is greatest, but at smaller angles the  $\lambda$  fundamental component is still significant. This results in a total curve which, whilst still smooth, has ‘kinks’ resulting from being a composite of two other curves which are, in this particular case, both significant to some extent. We first saw this result in Fig. 7(a) and the somewhat unusual shape of the calculated curve was indeed borne out by the experimental results. Close examination of Fig. 7(a) shows that this effect is apparent in some of the other curves, especially those involving rotating filters with high-atomic-number elements (Cu, Mo and Au). In the case of Fig. 7(b), the presence of 2 mm fixed *ex vacuo* Cu ensures that the  $\lambda/3$  harmonic is dominant for all rotated filters (at all angles) and so the curves are all smooth and dome-shaped.

## 5. Conclusion

We have demonstrated the utility of using accurate and comprehensive IC data sets collected for the transmission of an X-ray beam by a variety of rotating filters. The long-standing problem of inverting such data in order to derive the energy-dependent flux distribution is fundamentally ill-posed. We have shown, however, that our approach is quite robust and can yield valuable absolute results of considerable benefit. The method has been applied to both polychromatic and monochromatic X-ray beams of practical significance at IMBL, the latter incorporating harmonic contamination.

In the case of the polychromatic X-ray beam we have also made direct comparisons of our results with absorbed-dose measurements performed with a calibrated PinPoint ionization chamber, revealing excellent agreement. These results confirm our view that the discrepancies which are apparent in Fig. 4 are more closely associated with deficiencies of the theory than of the experiment itself. The detailed study for the monochromatic case enabled a quantitative assessment of the extent (to the fifth-order component) and magnitude of harmonic contamination present in the low-energy (25.3 keV) X-ray beam, and how this can be exacerbated when certain additional filtration is used. The level of harmonic contamination obtained experimentally has been shown to be in good agreement with detailed calculations which incorporate the (energy-dependent) integrated reflectivities associated with the bent-crystal DCLM.

## APPENDIX A

### Additional ADC IC and PinPoint measurements

An additional set of pink-beam measurements was collected in IMBL hutch 3B as a function of SCMPW field (12 fields from 0.80 to 4.00 T). The ADC and PinPoint ionization chambers already described were positioned side-by-side at 140.0 m from the source, and could be translated in and out of the X-ray beam quickly and accurately. In the case of the ADC IC,

a 5 mm × 5 mm W mask (4 mm thick) was translated into the X-ray beam at a distance of 139.0 m from the source, and for the PinPoint chamber a 20 mm × 20 mm W mask (also 4 mm thick) was used. Some additional shielding (especially in the horizontal direction) ensured that, when these masks were blocked, background readings were less than 0.2% of those for the primary beam. The SCMPW was taken through a full hysteresis loop ending at 0.00 T (and power supplies were turned off) prior to experiments starting. At this point, with the storage ring operating at 3.033 GeV, 200.0 mA and IMBL shutters open, no readings above normal background were recorded on the ionization chambers, *i.e.* no extraneous radiation, such as might be expected from adjacent bending magnets, was detected.

Accurate ionization-chamber measurements were recorded as a function of SCMPW field starting at 0.80 T and finishing at 4.00 T (including the ‘usual’ cases of 1.40, 2.00, 3.00 and 4.00 T). The first such measurements were with a ring current of 200 mA (‘top-up’ mode). The ring current was changed to approximately 20 mA at 1.40 T and 2 mA at 3.00 T (both ‘decay’ mode) to ensure that the ionization chambers continued to operate at acceptable signal levels. At the transition fields, measurements were recorded for both ring currents. The results presented here are all following scaling to a ring current of 200.0 mA. At each field value, data were collected for three different *in vacuo* filtrations, involving each of the downstream paddles (4 and 5) presenting (effectively) either  $2\sqrt{2}$  mm Al,  $\sqrt{2}$  mm Cu, or  $\sqrt{2}$  mm Al plus  $\sqrt{2}$  mm Mo to the X-ray beam, *i.e.* the two paddles always had, nominally, the same filters.

Each ionization-chamber reading was recorded three times and the values averaged; the electrometer readings for the PinPoint chamber were for 10 s each. The PinPoint readings were obtained with the most appropriate electrometer range (low or medium) and were processed as described in §4.1. The average values of air temperature and pressure in the experimental hutch (3B) were 21.6 (0.1)°C and 100490 (50) Pa, respectively, for which  $K_{TP}$  has the value 1.014. The value of  $K_Q$  used throughout this analysis was 0.99. The results are summarized in Fig. 9, with the %-differences of calculated *versus* experimental ionization-chamber readings plotted as a function of wiggler field. The plots are colour-coded according to the three *in vacuo* filtrations employed, with triangles representing 200 mA-ring-current results, squares representing 20 mA results, and diamonds representing 2 mA results (filled symbols for the ADC IC and not-filled symbols for the PinPoint chamber). The calculated values were obtained with *spec.exe*, as previously described, and allowing for all absorbing elements on the beamline. The selected field sizes for these calculations (with a spatial step size of 25  $\mu$ m) were 5.04 mm × 5.04 mm and 5.00 mm (H) × 2.00 mm (V) for the ADC IC and PinPoint, respectively. The former is the result of projecting the associated mask size from 139 m to 140 m, and the latter is dictated by the size of the active volume for the PinPoint chamber. The experimental ADC IC current values varied, after scaling to 200 mA ring current, from  $2.26 \times 10^{-11}$  A (for 0.80 T and the Cu-based

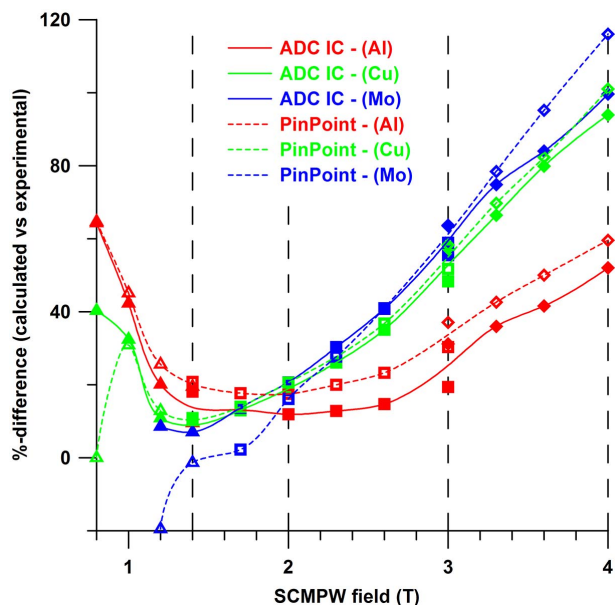


**Figure 9**  
 %-differences for calculated *versus* experimental ionization-chamber currents (ADC IC) and absorbed-dose rates to air (PinPoint chamber) as a function of SCMPW field. The results are provided for different *in vacuo* filtrations (Al-, Cu- and Mo-based), and were collected with different ring currents (200 mA up to and including 1.40 T denoted by triangles; 20 mA between and including 1.40 T and 3.00 T denoted by squares; 2 mA above and including 3.00 T denoted by diamonds). The dashed vertical lines mark the wiggler fields available to IMBL users (1.40, 2.00, 3.00 and 4.00 T). Further details are provided in the text.

*in vacuo* filtration; with no measurement being made for the Mo-based filtration) to  $1.27 \times 10^{-5}$  A (for 4.00 T and the Al-based *in vacuo* filtration; noting that the actual measurement was performed with 2 mA ring current). The experimental PinPoint dose-rate values (derived from charge values) varied from  $1.05 \text{ mGy s}^{-1}$  (for 0.80 T and the Cu-based *in vacuo* filtration) to  $369 \text{ Gy s}^{-1}$  (for 4.00 T and the Al-based *in vacuo* filtration).

It should also be pointed out that the *spec.exe* calculations of ADC IC currents make allowance for both ion-recombination and electron-loss effects as discussed by Stevenson *et al.* (2017), and involving the correction factors  $K_s$  and  $K_e$ , respectively. As an example, in the case of 3.00 T and the Al-based *in vacuo* filtration, the value of  $K_s$  was 1.073 for 20 mA ring current and 1.007 for 2 mA [for 200 mA (which was not used for this wiggler field),  $K_s$  would be 1.675]. The value of  $K_e$  in this case was 1.336, independent of ring-current value.<sup>19</sup>

The salient features of Fig. 9 are that: similar results are obtained for both ionization chambers; the vast majority of the %-differences are positive (that is, the calculated values of the IC currents and dose rates tend to overestimate the experimental values); for the wiggler fields used at IMBL (1.40 T and above), the %-differences tend to increase with field and with the hardness of the X-ray beam. These findings are, in general terms, quite consistent with those of Stevenson *et al.* (2017).

<sup>19</sup> We actually refer here to the effective electron-loss correction factor, as defined by Stevenson *et al.* (2017),  $K_{e,eff}$  in their terminology. The corresponding spectrally weighted value of  $K_e$  is 1.256.

## Acknowledgements

We thank the Accelerator Operators at the Australian Synchrotron for providing the special commissioning shifts (machine studies) needed for these experiments; Accelerator Scientists, especially Eugene Tan, and IMBL colleagues for stimulating and informative discussions. We acknowledge the generous financial support of NHMRC to key aspects of IMBL. One of us (FDiL) acknowledges support from the Australian Synchrotron, enabling an extended visit to IMBL during which a component of the experimental work reported here was undertaken. FDiL also acknowledges support from the MaXIMA project: ‘Three dimensional breast cancer models for X-ray imaging research’. This project has received funding from the European Union’s Horizon 2020 research and innovation programme under grant agreement No. 692097.

## References

Aoki, K. & Koyama, M. (1989). *Med. Phys.* **16**, 529–536.  
 Archer, B. R., Fewell, T. R. & Wagner, L. K. (1988). *Med. Phys.* **15**, 832–837.  
 Attix, F. H. (1986). *Introduction to Radiological Physics and Radiation Dosimetry*. New York: Wiley.  
 Ay, M. R., Shahriari, M., Sarkar, S., Adib, M. & Zaidi, H. (2004). *Phys. Med. Biol.* **49**, 4897–4917.  
 Baird, L. C. (1981). *Med. Phys.* **8**, 319–323.  
 Bell, G. E. (1936). *Br. J. Radiol.* **9**, 680–688.  
 Birch, R. & Marshall, M. (1979). *Phys. Med. Biol.* **24**, 505–517.  
 Boone, J. M. & Seibert, J. A. (1997). *Med. Phys.* **24**, 1661–1670.  
 Cao, J., Jiang, C.-Y., Zhao, Y.-F., Yang, Q.-W. & Yin, Z.-J. (2016). *Nucl. Sci. Technol.* **27**, 45.  
 Cho, T., Uehara, S., Yoshimura, A. & Yoshinaga, H. (1978). *Oral Surg.* **45**, 965–977.  
 Cruickshank, D. W. J. (1949). *Acta Cryst.* **2**, 65–82.  
 Drouin, D., Couture, A. R., Joly, D., Tastet, X., Aimez, V. & Gauvin, R. (2007). *Scanning*, **29**, 92–101.  
 Epp, E. R. & Weiss, H. (1966). *Phys. Med. Biol.* **11**, 225–238.  
 Erola, E., Eteläniemi, V., Suortti, P., Pattison, P. & Thomlinson, W. (1990). *J. Appl. Cryst.* **23**, 35–42.  
 Fewell, T. R. & Shuping, R. E. (1977). *Med. Phys.* **4**, 187–197.  
 Flegontova, E. Y., Bakaleinikov, L. A., Nam, K.-Y., Park, J. G., Kim, K.-W., Chon, K. S. & Yoon, K.-H. (2007). *J. Korean Phys. Soc.* **51**, 65–77.  
 Gabbai, M., Leichter, I., Mahgerefteh, S. & Sosna, J. (2015). *Acta Radiol.* **56**, 960–969.  
 Gallardo, S., Ródenas, J. & Verdú, G. (2004). *Med. Phys.* **31**, 2082–2090.  
 Gauvin, R., Lifshin, E., Demers, H., Horny, P. & Campbell, H. (2006). *Microsc. Microanal.* **12**, 49–64.  
 Greening, J. R. (1947). *Br. J. Radiol.* **20**, 71–78.  
 Greening, J. R. (1950). *Proc. Phys. Soc. A*, **63**, 1227–1234.  
 Greening, J. R. (1963). *Br. J. Radiol.* **36**, 363–371.  
 Hamilton, W. C. (1964). *Statistics in Physical Science; Estimation, Hypothesis Testing, and Least Squares*. New York: Ronald Press.  
 Hamilton, W. C. (1965). *Acta Cryst.* **18**, 502–510.  
 Harty, P. D., Lye, J. E., Ramanathan, G., Butler, D. J., Hall, C. J., Stevenson, A. W. & Johnston, P. N. (2014). *Med. Phys.* **41**, 052101.  
 Honkimäki, V., Sleight, J. & Suortti, P. (1990). *J. Appl. Cryst.* **23**, 412–417.  
 Honkimäki, V. & Suortti, P. (1992). *J. Appl. Cryst.* **25**, 97–104.  
 Hubbell, J. H. & Seltzer, S. M. (1995). *Tables of X-ray Mass Attenuation Coefficients and Mass Energy-Absorption Coefficients from 1 keV to 20 MeV for Elements Z = 1 to 92 and 48 Additional*

- Substances of Dosimetric Interest*. NIST Technical Report 5632. NIST, Bethesda, MD, USA.
- Hübner, W. (1958). *Fortschr. Röntgenstr.* **89**, 629–634.
- Israel, H. I., Lier, D. W. & Storm, E. (1971). *Nucl. Instrum. Methods*, **91**, 141–157.
- Jones, D. E. A. (1940). *Br. J. Radiol.* **13**, 95–101.
- Jones, D. E. A. (1961). *Br. J. Radiol.* **34**, 801–806.
- Levenberg, K. (1944). *Q. Appl. Math.* **2**, 164–168.
- Livingstone, J., Stevenson, A. W., Butler, D. J., Häusermann, D. & Adam, J.-F. (2016). *Med. Phys.* **43**, 4283–4293.
- Lye, J. E., Harty, P. D., Butler, D. J., Crosbie, J. C., Livingstone, J., Poole, C. M., Ramanathan, G., Wright, T. & Stevenson, A. W. (2016). *Phys. Med. Biol.* **61**, 4201–4222.
- McIntyre, G. J., Moss, G. & Barnea, Z. (1980). *Acta Cryst.* **A36**, 482–490.
- Manciu, M., Manciu, F. S., Vulcan, T., Nes, E. & Waggener, R. G. (2009). *J. X-ray Sci. Technol.* **17**, 85–99.
- Marquardt, D. W. (1963). *J. Soc. Ind. Appl. Math.* **11**, 431–441.
- Meyer, P., Buffard, E., Mertz, L., Kennel, C., Constantinesco, A. & Siffert, P. (2004). *Br. J. Radiol.* **77**, 224–230.
- Moffat, A. F. J. (1969). *Astron. Astrophys.* **3**, 455–461.
- Nowotny, R. & Höfer, A. (1985). *Fortschr. Röntgenstr.* **142**, 685–689.
- Pani, R., Laitano, R. F. & Pellegrini, R. (1987). *Phys. Med. Biol.* **32**, 1135–1149.
- Pearson, K. (1916). *Philos. Trans. R. Soc. A*, **216**, 429–457.
- Podgorsak, E. B. (2005). *Radiation Oncology Physics: A Handbook for Teachers and Students*. Vienna: IAEA.
- Sánchez del Río, M. & Dejus, R. J. (2011). *Proc. SPIE*, **8141**, 814115.
- Schulze, C. & Chapman, D. (1995). *Rev. Sci. Instrum.* **66**, 2220–2223.
- Schulze, C., Lienert, U., Hanfland, M., Lorenzen, M. & Zontone, F. (1998). *J. Synchrotron Rad.* **5**, 77–81.
- Sidky, E. Y., Yu, L., Pan, X., Zou, Y. & Vannier, M. (2005). *J. Appl. Phys.* **97**, 124701.
- Silberstein, L. (1932). *J. Opt. Soc. Am.* **22**, 265–280.
- Silberstein, L. (1933). *London Edinb. Dubl. Philos. Mag. J. Sci.* **15**, 375–394.
- Stevenson, A. W., Crosbie, J. C., Hall, C. J., Häusermann, D., Livingstone, J. & Lye, J. E. (2017). *J. Synchrotron Rad.* **24**, 110–141.
- Stevenson, A. W., Hall, C. J., Mayo, S. C., Häusermann, D., Maksimenko, A., Gureyev, T. E., Nesterets, Y. I., Wilkins, S. W. & Lewis, R. A. (2012). *J. Synchrotron Rad.* **19**, 728–750.
- Stevenson, A. W., Mayo, S. C., Häusermann, D., Maksimenko, A., Garrett, R. F., Hall, C. J., Wilkins, S. W., Lewis, R. A. & Myers, D. E. (2010). *J. Synchrotron Rad.* **17**, 75–80.
- Takahashi, T. & Watanabe, S. (2001). *IEEE Trans. Nucl. Sci.* **48**, 950–959.
- Tanaka, T. & Kitamura, H. (2001). *J. Synchrotron Rad.* **8**, 1221–1228.
- Tanaka, T. & Kitamura, H. (2007). *AIP Conf. Proc.* **879**, 355–358.
- Tanaka, T., Oura, M., Ohashi, H., Goto, S., Suzuki, Y. & Kitamura, H. (2000). *J. Appl. Phys.* **88**, 2101–2107.
- Tikhonov, A. N. & Arsenine, V. Y. (1977). *Solution of Ill-Posed Problems*. Washington: Winston. (Translated from Russian.)
- Tucker, D. M., Barnes, G. T. & Chakraborty, D. P. (1991). *Med. Phys.* **18**, 211–218.
- Van de Casteele, E., Van Dyck, D., Sijbers, J. & Raman, E. (2002). *Phys. Med. Biol.* **47**, 4181–4190.
- Young, R. A. & Wiles, D. B. (1982). *J. Appl. Cryst.* **15**, 430–438.